Original Research

Structural, Morphological, Optical and Dielectric Study along with Efficient Photocatalytic Activity of Dy^{3+} doped $ZnFe_2O_4$/g-C_3N_4 Composites for RhB Dye Degradation

Sania Arif [1], Hafeez Anwar [1,*], Khurram Ali [1], Muhammad Zahid [2]

[1] Department of Physics, University of Agriculture, Faisalabad 38040, Pakistan;
[2] Department of Chemistry, University of Agriculture, Faisalabad 38040, Pakistan
* Correspondence: hafeez.anwar@gmail.com

Received: November 18, 2025; Accepted: January 27, 2026

Abstract: Dye pollution harms the environment, but photocatalysis provides an eco-friendly remedy. Dy^{3+}-doped $ZnFe_2O_4$ with different weight ratios of g-C_3N_4 were synthesized via co-precipitation for RhB dye degradation. XRD confirmed a cubic structure with crystallite sizes of 20–30 nm, while SEM showed grain sizes of 8–24.5 nm. FTIR (650–4000 cm^{-1}) confirmed O–H, C–N, and C=N groups; UV–Vis showed band gaps of 1.98–1.74 eV. The dielectric constant peaked at low frequencies (31.6–3162 Hz), and AC conductivity reached $1.4 \times 10^{-6}(\Omega m)^{-1}$. Optimal photocatalytic performance was achieved at pH 8, 40 mg/100 mL catalyst dose, and 8 mM H_2O_2 using Dy^{3+}-doped $ZnFe_2O_4$ with composite g-C_3N_4 (0.4g), attaining ≈96.5% RhB degradation within 75 min. This composite showed good reusability over five cycles, confirming its high efficiency for water contaminant removal.

Keywords: co-precipitation; semiconductor materials; heterogeneous photocatalysis; wastewater treatment

1. Introduction

Clean water is essential for human survival. However, the rapid increase in organic pollutants has become a primary cause of global water contamination. Currently, nearly two billion people rely on polluted water sources, posing severe risks to public health. Herbicides, pesticides (such as chlordane and aldrin), and various industrial chemicals are major contributors to water pollution. Even at very low concentrations, these contaminants can cause serious health hazards, including carcinogenic and mutagenic effects [1–3].

Among organic pollutants, synthetic dyes are extensively used as colorants in numerous industrial applications, including textiles, paper, cosmetics, food additives, and laser printing. The uncontrolled discharge of these dyes into aquatic environments creates severe ecological problems, adversely affecting aquatic organisms and human health [4]. Rhodamine B (RhB) is a widely used xanthene dye in textile and food industries and is recognized for its high toxicity, non-biodegradability, and long-term persistence in water bodies. RhB obstructs light penetration in water, disrupts photosynthetic processes, and interferes with natural purification mechanisms, posing a significant threat to aquatic ecosystems and plant life [5,6]. Therefore, the complete removal of RhB from wastewater is critically important to mitigate its harmful environmental effects.

Various wastewater treatment methods, including ion exchange, membrane separation, evaporation, and advanced oxidation processes, have been explored for dye removal [7,8]. Among these, photocatalysis has attracted considerable attention due to its cost-effectiveness, operational

simplicity, and high degradation efficiency. Since the 1970s, hydroxyl-radical-based advanced oxidation processes (AOPs) have been widely employed for the degradation of non-biodegradable organic pollutants. In photocatalytic systems, a reusable semiconductor catalyst, light irradiation (preferably sunlight), and oxidizing agents such as oxygen or hydrogen peroxide are used to mineralize organic pollutants into harmless products [9,10].

Zinc-based semiconductors have been extensively investigated for photocatalytic applications. Zinc oxide (ZnO), for example, has shown promising performance in controlling water and air pollution, degrading organic contaminants, and enabling fuel generation from CO_2 and water [11,12]. Graphitic carbon nitride (g-C_3N_4) has also attracted significant interest due to its non-toxicity, suitable bandgap (~2.7 eV), chemical stability, and visible-light responsiveness. However, the practical application of pristine g-C_3N_4 is limited by its relatively low surface area and rapid recombination of photogenerated electron–hole pairs [13,14].

Another promising photocatalyst is zinc ferrite ($ZnFe_2O_4$), which exhibits low toxicity, visible-light absorption, structural stability, and magnetic recyclability [15]. Nevertheless, its photocatalytic performance is limited by rapid charge-carrier recombination. To overcome these limitations, rare-earth element doping has emerged as an effective strategy to tailor the electronic structure of photocatalysts. Rare-earth ions possess unique electronic configurations that can act as charge-trapping or mediating centers, thereby enhancing photocatalytic efficiency [16,17].

In this study, Dy^{3+}-doped $ZnFe_2O_4$ coupled with g-C_3N_4 is developed as an efficient visible-light-driven photocatalyst, where Dy^{3+} ions function as electron mediators to facilitate interfacial charge transfer and suppress recombination. Dy^{3+}-doped $ZnFe_2O_4$/g-C_3N_4 composites with different g-C_3N_4 weight ratios were synthesized via a co-precipitation method and applied for RhB dye degradation under solar irradiation. The synthesized materials were systematically characterized using XRD, SEM/EDX, FTIR, UV-Vis spectroscopy, and dielectric analysis to examine their structural, morphological, optical, and electrical properties. The results demonstrate that coupling Dy^{3+}-doped $ZnFe_2O_4$ with g-C_3N_4 significantly enhances visible-light absorption and promotes efficient separation and transport of photogenerated charge carriers. The photocatalytic performance was evaluated under various operational parameters, including pH, catalyst dosage, H_2O_2 concentration, reaction time, and light exposure. The improved degradation efficiency of the optimized composite highlights the synergistic effect of rare-earth doping and heterojunction formation, offering a promising approach for sustainable wastewater treatment.

2. Materials and methods

2.1. Chemicals

All the chemicals were purchased from Sigma-Aldrich/Merck and used without additional purification. Zinc nitrate hexahydrate [$Zn(NO_3)_2{\cdot}6H_2O$] (95.0%), Iron nitrate hexahydrate [$Fe(NO_3)_2{\cdot}6H_2O$] (98.01%), Dysprosium nitrate [$Dy(NO_3)_2.6H_2O$] (99%), Ethanol, Sodium hydroxide [NaOH] (99.99%) and melamine were used as precursors and RhB dye was used for photocatalytic degradation process.

2.2. Synthesis of g-C_3N_4

The process of thermal polymerization was employed to make g-C_3N_4. 10 g of melamine was added to a crucible and heated to 550 °C for three hours. This heating process burned the melamine in the furnace, resulting in the production of yellow colored g-C_3N_4.

2.3. Synthesis of Dy-$ZnFe_2O_4$

A stoichiometric ratio of $Zn_{1-x}Dy_xFe_2O_4$ [x = 0.03], was used to dissolve zinc nitrate hexahydrate, dysprosium nitrate, and ferric nitrate in 50 ml of distilled water. Throughout the process of synthesis, solutions were constantly stirred to attain homogeneity and drops of the precipitating agent (NaOH) were added to reach and maintain pH 8. After that, the solution was

heated to 80 °C for one hour. The brown-colored precipitates were formed after undergoing two rounds of centrifugation (first with double-distilled water to remove impurities, followed by ethanol to remove nitrate ions). After being dried at 70 °C for 12 h, the resulting product was analyzed. The final product was ground into fine nanoparticles and the resulting powder was subsequently calcined in a muffle furnace at 500 °C for three hours.

2.4. Synthesis of Dy-$ZnFe_2O_4$/g-C_3N_4

The Co-precipitation method was used to produce the Dy-$ZnFe_2O_4$/g-C_3N_4 composites depicted in Figure 1. To attain homogeneous solutions, 0.2 g of Dy-$ZnFe_2O_4$ and 0.2 g of g-C_3N_4 were first separately dispersed in 50 mL of water. After 15 min of mixing and combining the solutions, the suspension was sonicated for another 15 min to make sure it was evenly distributed. After adding the g-C_3N_4 solution dropwise to the Dy-$ZnFe_2O_4$ solution, the mixture was allowed to stirred at room temperature for half an hour.

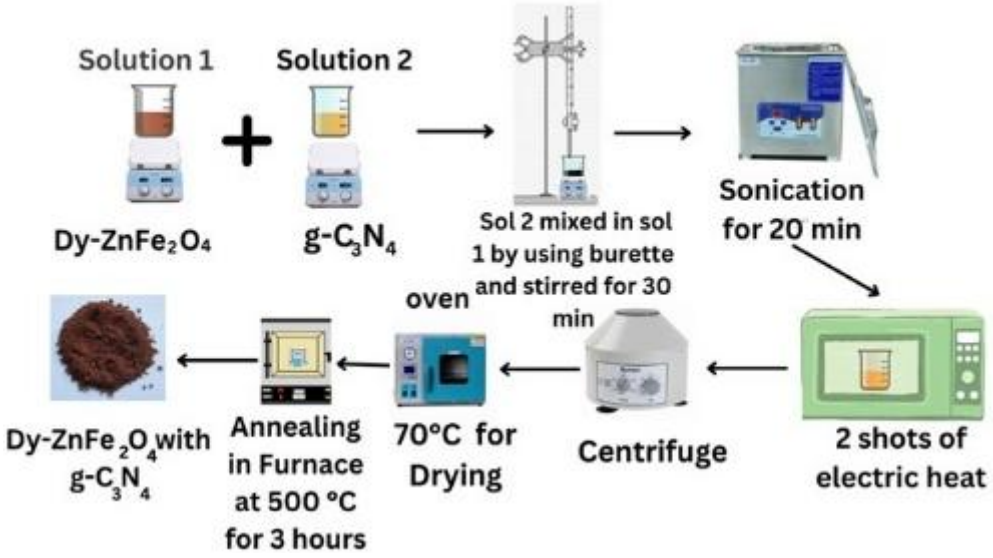

Figure 1. Schematic diagram for the synthesis of Dy^{3+} doped $ZnFe_2O_4$/g-C_3N_4.

The resultant solution was then sonicated for an additional 15 min. After that, the solution underwent centrifugation (5000 rpm) for 10 min and was washed three times with distilled water, followed by ethanol washing to remove residual nitrates. The gathered material was then dried in an oven at 70 °C overnight. The final product was converted into fine powder. The final product was ground into fine nanoparticles, and the resulting powder was subsequently calcined in a muffle furnace at 500 °C with heating rate of 5 °C min^{-1}, resulting in a brown-colored powder. By changing the weight ratios of g-C_3N_4-X (X = 0.2, 0.3, 0.4), the samples were named as DZG1, DZG2, and DZG3, respectively. Table 1 compares the co-precipitation conditions and parameters used in this work with those reported in previous studies.

Table 1. Comparison of current co-precipitation method conditions/parameters with literature.

Material/Composite	Synthesis Method	Temperature (°C)	Duration (h)	Crystallite size (nm)	SSA (m^2/g)	Ref
$ZnFe_2O_4$/Ag	Co-precipitation	80	2	10	64	[18]
$ZnFe_2O_4$/Ag/AgBr	Co-precipitation	90	3	30	48	[19]
$ZnFe_2O_4$/TiO_2	Co-precipitation	75	3.5	22	45	[20]

$ZnFe_2O_4$/CNT	Co-precipitation	95	2	18	60	[21]
$ZnFe_2O_4/SiO_2$	Co-precipitation	70	4	25	50	[22]
$ZnFe_2O_4/MnO_2$	Co-precipitation	85	3	26	47	[9]
$ZnFe_2O_4$/NiO	Co-precipitation	90	3.5	29	61	[13]
Dy^{3+}-$ZnFe_2O_4$	Co-precipitation	80	2	18	62	[23]
Dy^{3+}-$ZnFe_2O_4$/g-C_3N_4	Co-precipitation	80	75 min	24.05	12.74	Present work

2.5. Photocatalytic activity

To assess the photocatalytic activity, 50 mL solution of RhB was prepared. To determine the equilibrium between desorption and adsorption of the photocatalyst and dye solution, 20 mg and 30 mg of the photocatalyst were separately added to 50 mL of RhB solution. Both samples were then kept in the dark for 30 min to allow equilibrium to be established. The pH was adjusted by using 1 M of NaOH and 0.1 M of HCl solutions. After 30 min in the dark, an oxidant (H_2O_2) solution was added. Then, the whole setup was exposed to sunlight irradiation between 11:00 and 14:00 h under strong sunlight. Using a LUX meter, the intensity of sunlight (1080 W m^{-2}) was measured, with ambient temperatures ranging from 35 °C to 40 °C. After centrifuging for 15 min, 5 mL solution was taken and absorbance was determined from UV-Vis spectroscopy. The efficiency was determined by using Equation (1):

$$\text{Photocatalytic efficiency } (\eta) = (1 - \frac{C_t}{C_0}) \times 100 \quad (1)$$

The dye concentration is indicated by C_t after time 't' and C_0 indicates initial concentration.

3. Characterization

Diffraction patterns of the synthesized Dy^{3+} doped $ZnFe_2O_4$ with different contents of g-C_3N_4 were captured using the X-ray diffraction (XRD), which had a precise wavelength (λ) of 0.154 nm and covered a 2θ range from 20° to 80°. Morphological characterization was carried out using a JEOL-JSM 5910 scanning electron microscope (SEM) to examine the surface structure of the materials. The absorption bands were identified and checked using a [Perkin Elmer] FTIR spectrometer. A UV-visible spectrometer (PG Model T-80) was used to perform optical measurements in the wavelength range of 250–750 nm to examine the optical characteristics of the composites. Dielectric evaluations were taken at RT with a 3536 series LCR meter.

4. Results and discussions

4.1. XRD analysis

XRD investigation was utilized to estimate the phase and structural information of the synthesized Dy^{3+} doped $ZnFe_2O_4$ with g-C_3N_4 composites. Figure 2(a) shows the patterns of XRD of Dy^{3+}-doped $ZnFe_2O_4$ with different content of g-C_3N_4. In XRD spectra, the diffraction peaks were seen at 2θ = 29.69°, 35.88°, 43.19°, 57.25°, 62.91° and indexed with (220), (311), (400), (511), (440) with the JCPDS card data 82–1012, which showed the cubic structure. The Dy^{3+} doped $ZnFe_2O_4$ with g-C_3N_4 structure is successfully obtained, as demonstrated by the strong interaction between g-C_3N_4 and $ZnFe_2O_4$. As the mass percentage of g-C_3N_4 increased, g-C_3N_4 diffraction peaks gradually

increased. The crystallite size of a Dy^{3+} doped $ZnFe_2O_4$ with g-C_3N_4 composite is estimated using the Debye-Scherrer equation [24,25]:

$$D = \frac{k\lambda}{\beta\cos\theta} \tag{2}$$

where D is the crystallite size, k represents the Scherrer constant (typically 0.9), λ is the wavelength of X-ray (1.54 Å), β is the full width at half maximum (FWHM) in radians and θ is the diffraction angle measured from the 2θ scale.

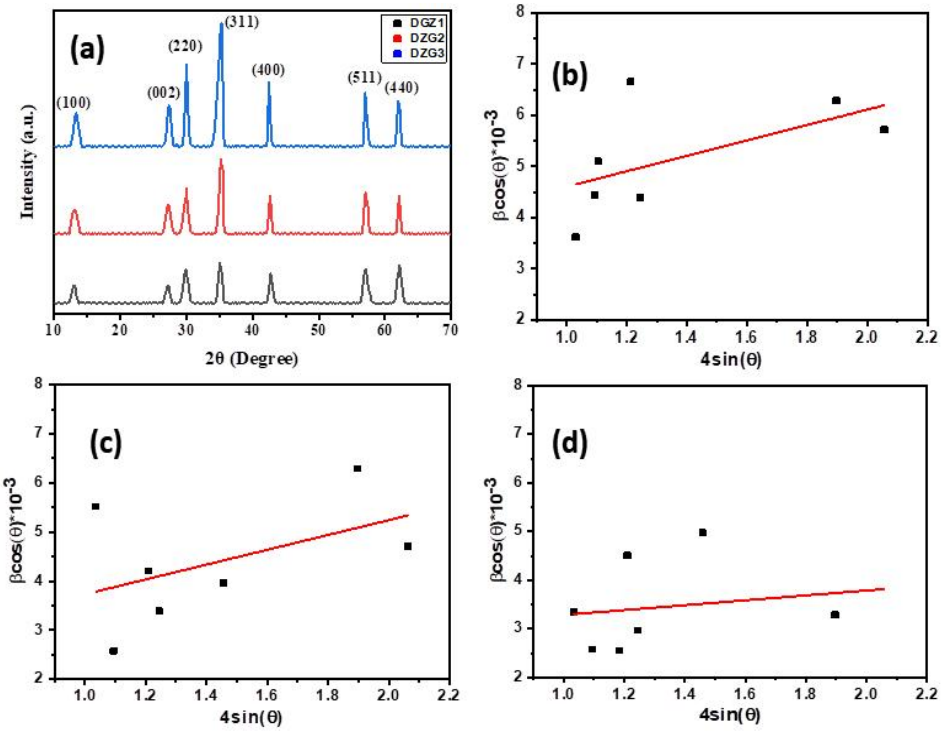

Figure 2. (a) XRD pattern, W–H plots of Dy^{3+} doped $ZnFe_2O_4$/g-C_3N_4 nanocomposites; (b) DZG1; (c) DZG2; (d) DZG3.

The crystallite size decreases from 28.25 nm (DZG1) to 16.51 nm (DZG3), indicating that the addition of more amount of g-C_3N_4, leads to smaller crystalline domains. This may result from g-C_3N_4 acting as a growth inhibitor, limiting crystallite growth. This calculation also aided in determining the lattice parameters a, b and c, assuming cubic symmetry where a = b = c.

$$a = \frac{d}{\sqrt{(h^2 + k^2 + l^2)}} \tag{3}$$

where Miller indices, h, k and l indicate lattice parameters of a and d is the d spacing. The lattice parameter decreases from 8.41 Å (DZG1) to 8.28 Å (DZG3). Bragg's law can be used to calculate the d spacing (Equation (4)).

$$2d\sin\theta = n\lambda \tag{4}$$

The d-spacing decreases slightly from 2.60 Å (DZG1) to 2.53 Å (DZG3). Equation (5) is used to calculate the unit cell volume (V) for the cubic system based on the lattice parameter [26]:

$$V = a^3 \tag{5}$$

As the lattice parameter decreases, the unit cell volume drops from 594.8 Å3 (DZG1) to 567.7 Å3 (DZG3). As g-C_3N_4 alters the structural framework, this trend shows the packing of atoms into the crystal lattice. The following formula (Equation (6)) was employed to confirm the X-ray density (XRD) of the prepared samples:

$$\rho_{\mathrm{XRD}} = \frac{NM_w}{N_{\mathrm{A}}V} \tag{6}$$

Here, N indicates the quantity of atoms in the cubic lattice cell, Avogadro's number is represented by N_{A}, and the molecular weight of the prepared composites is indicated by Mw and V represents the volume of each unit cell.

The peaks in the XRD spectrum are indicative of an excessive nanocrystalline composition. The (M.I) is derived from the Full Width at Half Maximum (FWHM) of the XRD information. The morphological index (M.I) is determined by analyzing the full width at half maximum (FWHM) of peaks. The following equation (Equation (7)) is used to quantify the morphological index.

$$\text{Morphological Index} = \frac{\mathrm{FWHM}_h}{\mathrm{FWHM}_h + \mathrm{FWHM}_p} \tag{7}$$

Here, FWHM_h and FWHM_p represent the full width at half maximum of the highest and specific peaks of crystalline, respectively. The morphological index for Dy^{3+} doped $ZnFe_2O_4$ with g-C_3N_4 is presented in Table 2. The morphological index (M.I.) is used as a qualitative comparative parameter to assess relative changes in particle morphology and surface irregularity among prepared samples. A higher M.I. value indicates increased peak broadening, which is generally associated with smaller crystallite size, greater surface irregularity, or higher defect density. Although M.I. is not a direct measure of surface area or porosity and does not substitute techniques such as BET analysis, it serves as a supplementary indicator for comparing relative morphological variations in samples synthesized under similar conditions. In this study, the observed variation in M.I. supports the SEM observations and helps explain trends in photocatalytic activity through its indirect relation to surface-active sites.

Micro-strain is determined using Equation (8) [27]:

$$\beta = 4 \times \varepsilon \times \tan\theta \tag{8}$$

For Williamson-Hall analysis, the detected peak broadening is the sum of Equation (2,8) and is expressed as:

$$\beta\cos\theta = \left(\frac{0.9\lambda}{D}\right) + (4 \times \mathrm{Strain} \times \sin\theta) \tag{9}$$

The relationship between $\beta\cos\theta$ and $4\sin\theta$ shows the slope value, which is represented by the straight line. The W–H plots of Dy^{3+} doped $ZnFe_2O_4$/g-C_3N_4 nanocomposites (DZG1, DZG2, and DZG3) as depicted in Figure 2(b–d). It is noted that W–H plots exhibit a certain degree of data scattering. This behavior is attributed to the nanocrystalline nature of the Dy^{3+} doped $ZnFe_2O_4$/g-C_3N_4 nanocomposites and the simultaneous contribution of multiple peak-broadening factors, including crystallite size reduction, lattice strain, doping induced lattice distortion, and interfacial strain introduced by g-C_3N_4 coupling. Such non-ideal linearity in W–H plots is commonly observed in ferrite-based nanocomposite systems. Therefore, the W–H analysis is employed to estimate average effective crystallite size and to enable comparative evaluation among samples synthesized under similar conditions. The difference arises because the Scherrer equation, unlike the Williamson-Hall method, considers only size broadening. In contrast, the Williamson-Hall method includes both crystallite size and lattice strain. Figure 2(b–d) shows the micro-strain calculated from the slope values. The formula was used to calculate the SSA [28]:

$$\mathrm{SSA} = \frac{6}{\rho_{\mathrm{XRD}}} \times D \tag{10}$$

Dislocation density, which significantly impacts crystallographic properties, can be calculated from Equation (11) [29]:

$$\delta = \frac{1}{D^2} \tag{11}$$

Strain is calculated by Equation (12):

$$\varepsilon = \frac{1}{d^2} \tag{12}$$

The variation in XRD parameters for Dy^{3+} doped $ZnFe_2O_4$ with different contents of g-C_3N_4 nanocomposites is due to lattice distortions from Dy^{3+} doping, phase interactions with g-C_3N_4 and resulting changes. These factors can cause shifts in peak positions, changes in crystallite size and variations in peak intensity and broadening.

Table 2. Structural parameters calculated from XRD results.

Sample name	DZG1	DZG2	DZG3
***d*-spacing (Å)**	2.60	2.54	2.53
D (nm) from Scherrer's equation	28.25	17.26	16.51
D (nm) from (W–H plot)	36.31	26.43	20.02
Lattice parameter (a = b = c)	8.41	8.34	8.28
V (Å^3)	594.8	580.1	567.7
Morphological Index (M.I)	1.55	1.3	1.24
X-ray density ϱ_{XRD} (g/cm^3)	1.33	1.35	1.36
SSA(m^2/g)	159.7	257.5	267.3
Dislocation density × 10^4 (m^{-2})	1.25	3.35	3.6
Strain ε	14.2	15.4	15.6

4.2. SEM analysis

The morphological analysis of Dy^{3+} doped $ZnFe_2O_4$ with g-C_3N_4 composites were determined through SEM. SEM analysis of Dy^{3+} doped $ZnFe_2O_4$ with g-C_3N_4 composites shows that Dy^{3+} doping alters surface morphology, affecting grain structures and particle sizes due to changes in growth kinetics. The incorporation of g-C_3N_4 in Dy^{3+} doped $ZnFe_2O_4$ enhanced surface area and improved particle dispersion, as shown in Figure 3(a–c). The size, shape, aggregation and overall distribution of particles have all changed due to g-C_3N_4 [30]. The increased presence of water and reducing agents among ferrite particles can be attributed to their agglomeration, likely caused by the magnetic attraction between the particles. The average grain sizes of the prepared composites were determined to be 8 nm, 13 nm, and 24.15 nm using ImageJ. It is observed that SEM-derived crystallite sizes are smaller than XRD-derived crystallite sizes due to particle aggregation, polycrystalline nature, and projection effects inherent to SEM imaging.

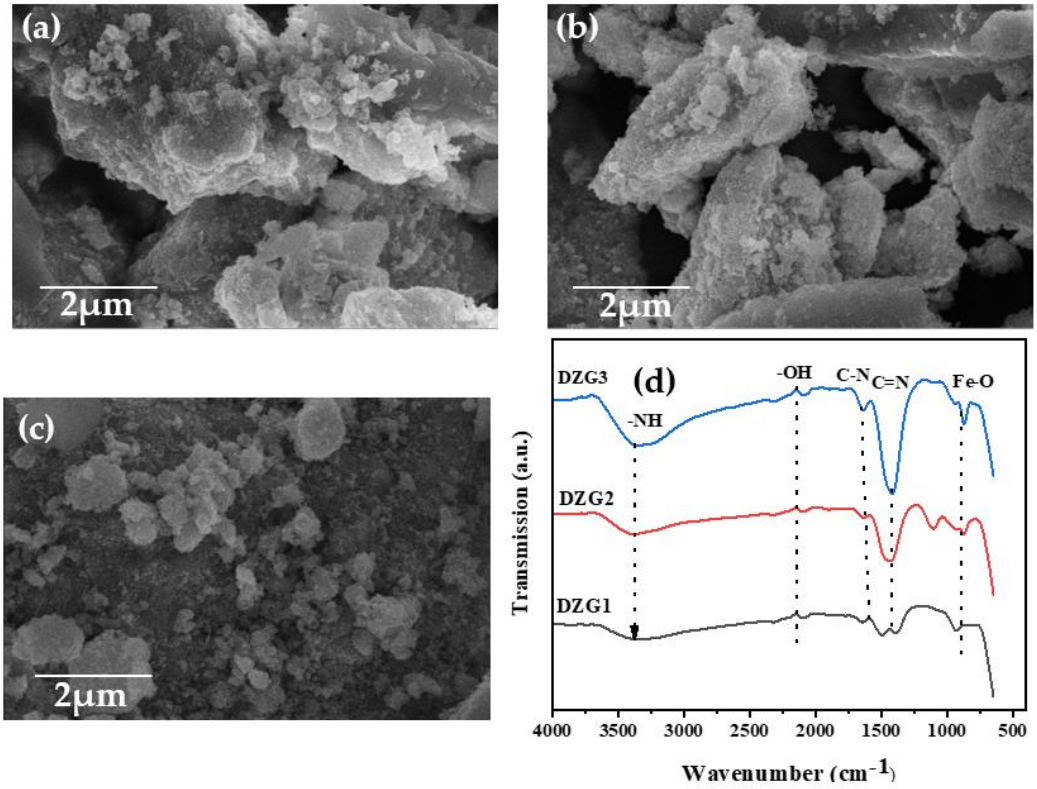

Figure 3. SEM micrographs of Dy^{3+} doped $ZnFe_2O_4$/g-C_3N_4 nanocomposites (a) DZG1; (b) DZG2; and (c) DZG3 ; (d) FTIR of Dy^{3+} doped $ZnFe_2O_4$/g-C_3N_4 nanocomposites DZG1, DZG2, DZG3.

4.3. FT-IR analysis

For identifying functional groups in prepared composites, FTIR is the most effective and dynamic method available. Figure 3(d) shows the FTIR characteristic peaks of Dy^{3+} doped $ZnFe_2O_4$ with g-C_3N_4 in the range of 650–4000 cm^{-1} [31]. The FT-IR spectra reveal that the triazine units are responsible for the peak at 804 cm^{-1}, while the C–N and C=N are linked to the peaks at 1411 and 1645 cm^{-1}, respectively shown In Table 3. The absorptions of some bands at 590 cm^{-1}, are associated with the Fe–O, at 2620 cm^{-1} demonstrating the OH groups' stretching vibration. The absorption band observed at 1630 cm^{-1} and 3460 cm^{-1}, is attributed to the stretching and bending of the O–H bonds of the adsorbed H_2O molecules.

Table 3. Summarizing all FTIR peaks.

Wavenumber (cm^{-1})	Assignment	Reference
~804	Triazine ring breathing	[35]
~1411	C–N stretching	[35]
~1645	C=N stretching	[35]
~590	Fe–O vibration	[35]
~3460	O–H stretching	[35]

4.4. UV-visible spectroscopy analysis

The characteristics of the optical of semiconducting nanomaterials were examined using UV–visible spectra [32,33]. Figure 4(a) displays the band gap and absorption spectrum for the

synthesized Dy^{3+} doped $ZnFe_2O_4$ with g-C_3N_4 over the wavelength range of 300–800 nm. The optical bandgap (E_g) of material can be computed using a Tauc plot assuming an indirect allowed transition (n = 2), as shown in Figure 4(b–d). Equation (13) is utilized to determine the optical band gap [34].

$$\alpha hv = A\left(hv - E_g\right)^n \tag{13}$$

The (α) absorption coefficient was estimated in cm^{-1}, the characteristic parameter is represented by (A), Planck's constant denotes (h) and (n) are specified with the transition process.

The band gap values at different contents of g-C_3N_4 nanocomposites are determined as 1.98 eV, 1.86 eV and 1.74 eV, as shown in Figure 4(b–d), respectively. First, Dy^{3+} ions introduce localized 4f electronic states within the band structure, acting as shallow trapping centers and facilitating sub-bandgap electronic transitions. Second, the formation of a $ZnFe_2O_4$/g-C_3N_4 heterojunction results in favorable band alignment, enabling efficient charge transfer at the interface and lowering the effective excitation energy. Third, Dy^{3+} substitution and interfacial interactions generate defect-related states, such as oxygen vacancies, which further contribute to band tailing and enhanced visible-light absorption. Overall, these effects improve photon utilization and enhance photocatalytic activity under solar irradiation.

The Tauc plots of Dy^{3+}-doped $ZnFe_2O_4$/g-C_3N_4 composites exhibit two distinct linear regions, indicating the presence of multiple optical transitions. The higher-energy slope corresponds to the fundamental band-to-band transition, while the lower-energy slope originates from sub-bandgap transitions associated with Dy^{3+} 4f localized states, oxygen vacancies, and interfacial defect levels introduced by g-C_3N_4 coupling. These defect-related states contribute to enhanced visible-light absorption and improved photocatalytic activity. The reported band-gap values are extracted from the dominant absorption edge relevant to photocatalytic performance under solar irradiation [36,37].

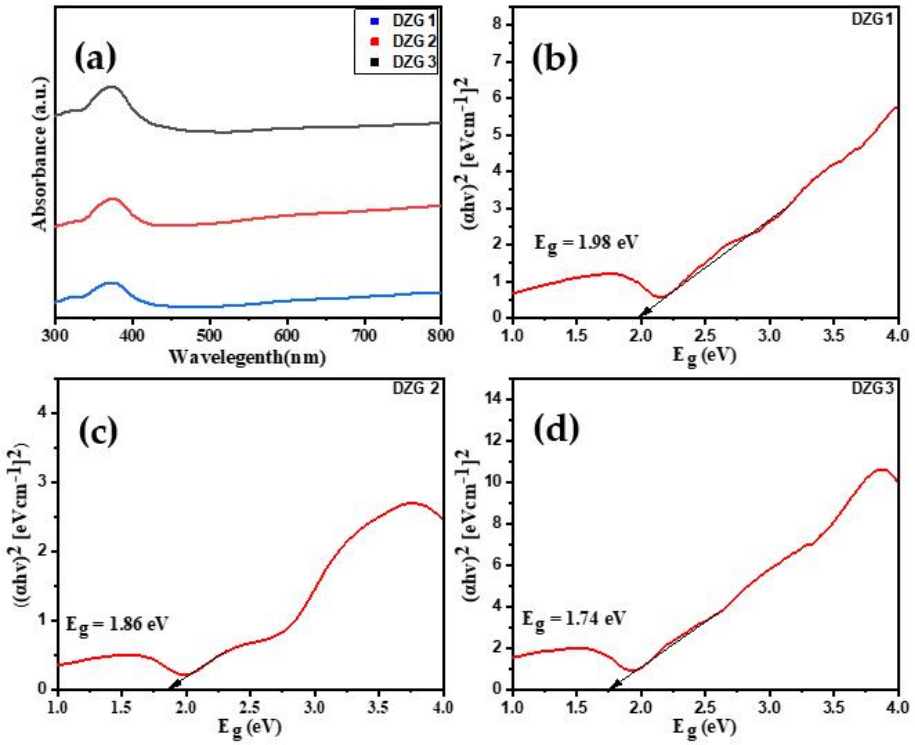

Figure 4. (a) UV-Vis spectrum; (b)–(d) Tauc's plot of Dy^{3+} doped $ZnFe_2O_4$/g-C_3N_4 nanocomposites (DZG1, DZG2, and DZG3).

4.5. Dielectric properties

The real part of dielectric permittivity (ε') represents the material's ability to retain electric polarization, while the imaginary part (ε'') reflects its capacity to dissipate power through electric loss [38]. The following formula is used to calculate ε':

$$\varepsilon' = \frac{ct}{A\epsilon_0} \tag{14}$$

Here, "c", "t" and "A" indicate capacitance, thickness and surface area of pellet, ε_0 is the permittivity of free space having value 8.85×10^{-12} $m^{-3}kg^{-1}s^4A^2$. The loss factor of a dielectric material (ε'') is calculated from Equation (15):

$$\varepsilon'' = \tan\delta \times \varepsilon' \tag{15}$$

Here, ε'' denotes the loss factor, while δ indicates the loss angle [39,40]. The dielectric constant (ε') varies with applied frequency, as shown in Figure 5(a). In Dy^{3+} doped $ZnFe_2O_4$/g-C_3N_4 nanocomposites (DZG1, DZG2, and DZG3), dielectric constant values increased with increasing g-C_3N_4 content. Figure 5(b) shows the relation between the dielectric loss factor (ε'') with log f. With increasing frequency, the decrease in dielectric constant and loss indicates improved charge carrier mobility and reduced polarization lag, favoring efficient electron hopping between Fe^{2+}/Fe^{3+} sites. The DZG3 composite exhibits comparatively higher dielectric permittivity and lower impedance, reflecting enhanced charge transport and reduced recombination probability. These dielectric characteristics directly support the improved photocatalytic efficiency of DZG3 by facilitating effective separation and migration of photogenerated charge carriers.

The following formula can be used to determine the dielectric material's tangent loss (δ) [41].

$$\text{Tan}\,(\delta) = \frac{1}{2\pi fRC} \tag{16}$$

The variation of tangent loss (δ) with frequency is illustrated in Figure 5(c). Notably, the tangent loss peaks at lower frequencies, indicating that higher material levels contribute to greater energy dissipation as heat.

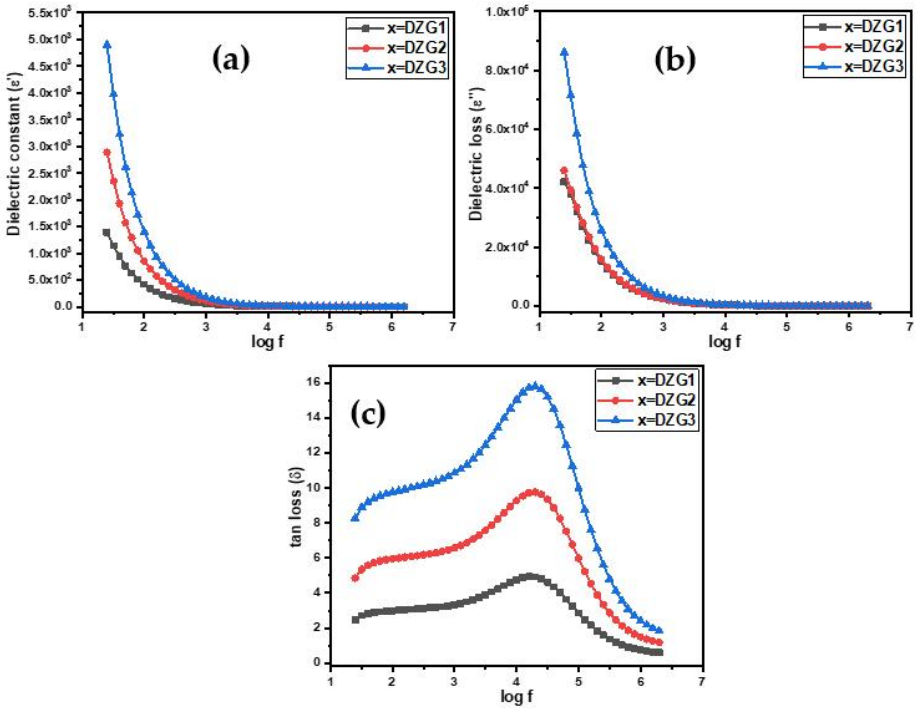

Figure 5. Log f verses (a) ε'; (b) ε''; (c) tan loss (δ) Dy^{3+} doped $ZnFe_2O_4$/g-C_3N_4 nanocomposites (DZG1, DZG2, and DZG3).

The conductivity of the material is determined using the formula:

$$\sigma = \sigma_{ac} + \sigma_{dc} \tag{17}$$

The second term on the right side of Equation (17), referred to as DC conductivity, remains invariant with frequency. In contrast, the first term, known as AC conductivity, varies with frequency and can be calculated using the Equation (18):

$$\sigma_{ac} = \pi f \varepsilon'' \varepsilon_0 \tag{18}$$

Here, ε'' stands for the imaginary part of the dielectric constant and ε_0 for the permittivity of free space. For prepared composites, the variation of AC conductivity with the log f is shown in Figure 6(a). Plotting the graph of $\log(\sigma_{ac})$ versus $\log(\omega)$, as illustrated in Figure 6(b), enables the determination of the exponent "n" through the relation (Equation (19)):

$$\sigma(\omega) = B \times \omega^n \tag{19}$$

With an intercept equal to log B at log ω = 0 and a slope equal to the exponent "n", the plot of $\log(\sigma_{ac})$ against $\log(\omega)$, shows a nearly constant relationship. The value of 'n' ranges between 0 and 1. When "n" equals 0, electrical conduction remains independent of frequency. Conversely, as "n" approaches value greater than 0 but less than or equal to 1, electrical conduction becomes frequency dependent. The prepared samples exhibit frequency-dependent behaviour, as indicated by the exponent values which range from 0.10 to 0.15.

For Dy^{3+} doped $ZnFe_2O_4$/g-C_3N_4 nanocomposites (DZG1, DZG2, and DZG3) composites, Figure 6(c,d) show the complex and electrical modulus (M' and M'') varies with the log ω. The complex and electrical modulus, calculated using the equations below, are essential for determining the total electrical modulus (M_{total}):

$$M_{total} = M' + jM'' \tag{20}$$

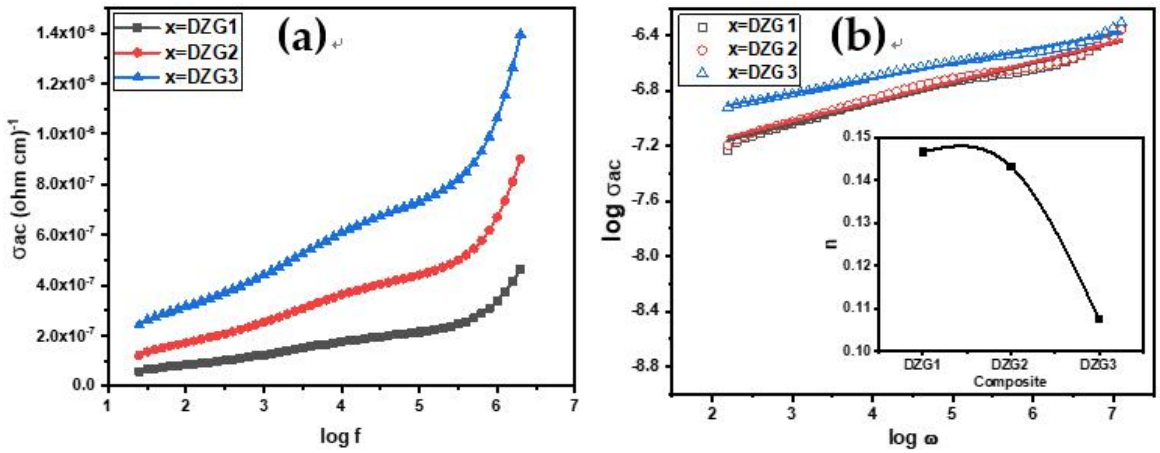

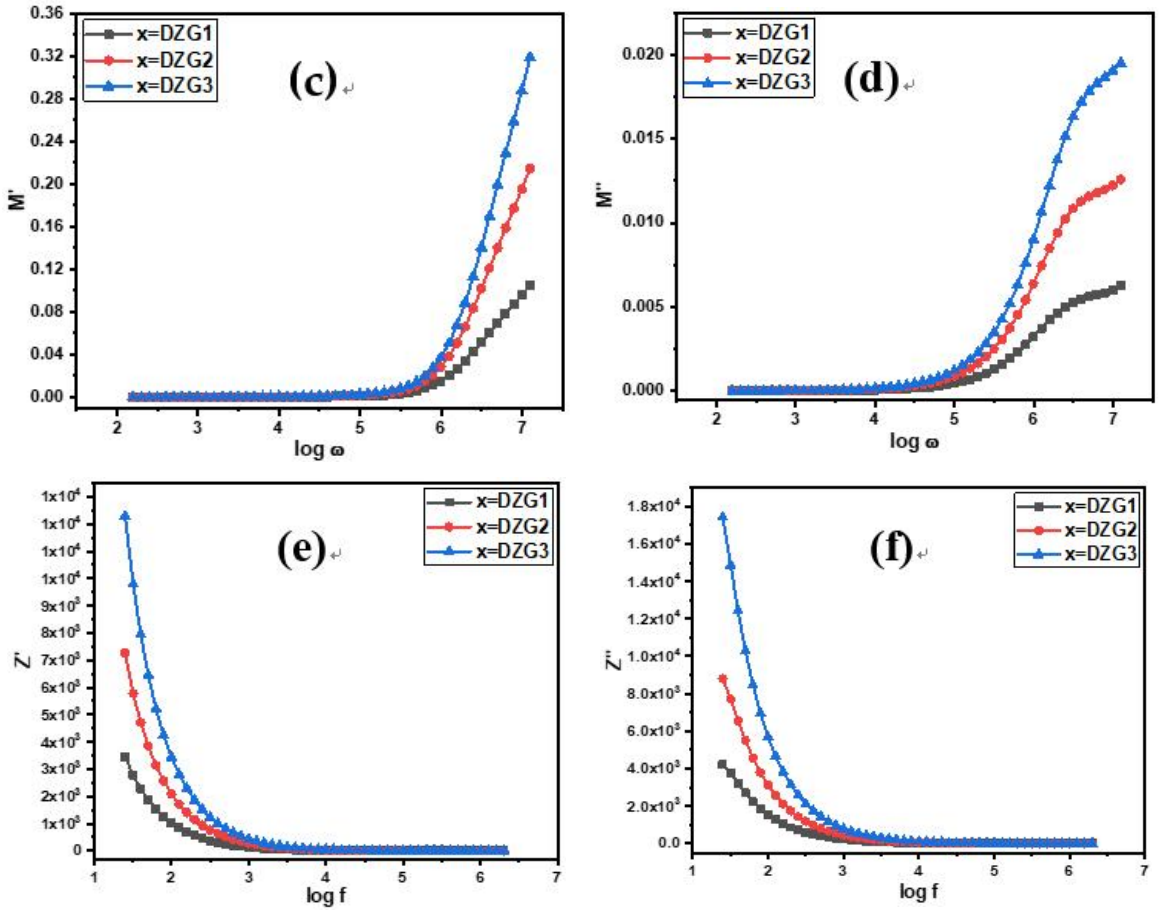

Figure 6. Frequency verses (a) σ_{ac}; (b) log σ_{ac} vs. log ω (dotted line and solid line represent experimental and linear fit, respectively), inset: Frequency exponent "n" vs. composites; (c) M; (d) M; (e) Z; (f) Z of Dy^{3+} doped $ZnFe_2O_4$/g-C_3N_4 nanocomposites (DZG1, DZG2, and DZG3).

Equation (21) can be used to calculate the first factor in the above equation:

$$M' = \frac{\varepsilon'}{\varepsilon'^2 + \varepsilon''^2} \tag{21}$$

Equation (22) can be used to find the second factor in Equation (20):

$$M'' = \frac{\varepsilon''}{\varepsilon'^2 + \varepsilon''^2} \tag{22}$$

Both complex and electrical modulus at lower frequencies retain a constant value, which can be attributed to the ionic polarization, as illustrated in Figure 6(e,f) [42]. The variation of the frequency-dependent real part of impedance (Z') is depicted in Figure 6(e). The impedance can be computed using the following relation, taking into account both its real and imaginary parts [43]:

$$Z = Z' + jZ'' \tag{23}$$

where Z' stands for the complex impedance's resistive component and Z'' for its reactive component. Grain boundaries play a major role in the higher values of impedance (Z') at lower frequencies; however, as frequency increases, this influence decreases. Notably, the substitution of Dy^{3+} ions lead to a reduction in Z', showing an improvement in the material's conductivity at minimum frequencies. Figure 6(f) shows the relationship between frequency and the imaginary part (Z'') of impedance. At lower frequencies, the value of Z'' increases with the substitution of Dy

ions. Furthermore, a greater Z'' value and a general rise in material impedance (Z'') resulted from additional increases in Dy content.

4.6. Effect of different parameters on RhB degradation

The efficiency of the photocatalyst in degrading RhB under sunlight is directly affected by pH amount of the solution. The research is carried out to evaluate the effect of pH on the degradation of RhB. For this purpose, at various pH ranges of 2–9, the ability of the photocatalyst degradation of RhB was checked. Diluted HCl or NaOH is used to change the pH of the solution. Due to the formation of aromatic hydroxylase species, the degradation efficiency of RhB decreased at *pH* values (i.e., 9). The condition of optimum pH is essential for preventing the wastage of excess amount of catalyst and maximizing the absorption of visible light for improved photodegradation [44]. Dy^{3+} doped $ZnFe_2O_4$/g-C_3N_4 nanocomposites (DZG1, DZG2, and DZG3) for DZG3 exhibits a maximum degradation efficiency of 96.5% at pH 8 within 75 min as shown in Figure 7(a). The enhanced performance was attributed to the increased availability of active sites, efficient charge separation facilitated by Dy^{3+} doping and the strong adsorption of RhB at the catalyst surface. The production of hydroxyl radicals (•OH), which are essential for the degradation process, is encouraged by the slightly alkaline pH 8 environment while the radicals seen at higher pH levels (such as pH 9) are reduced. This optimal pH condition ensures efficient visible light absorption and prevents excessive catalyst consumption, highlighting the significance of tailoring reaction parameters for practical water purification applications.

The efficiency of RhB dye degradation increased for all catalysts, but especially for DZG3, when the catalyst dosage was raised from 10 to 80 mg for 50ml of dye solution at pH 8 and exposed to radiation for 75 min, as Figure 7(b) illustrates. The more catalyst load there were, the more active sites there were on the photocatalytic surface, which led to an increase in hydroxyl radicals. The photo degradation efficiency of prepared material at different concentrations were enhanced from 70% to 96.5% as the composite dosage was enhanced from 10 to 40 mg. Additionally, it was noted that a continued rise in photocatalyst dosage led to a decrease in degradation efficiency in all samples. The reason for this is that as the catalyst dose increases, the number of active sites much enhanced causing penetration of light slow due to shielding effect.

To optimize the oxidant dose, the concentration of H_2O_2 varied from 2 to 14 mM. The impact of oxidant dosage on dye degradation is studied using prepared composites Figure 7(c) demonstrates that increasing the oxidant dose causes degradation to increase up to a point, after which it begins to decrease. The optimization process of H_2O_2 was carried out by following experimental conditions such as pH = 5, catalyst dosage = 40 mg Dy^{3+} doped $ZnFe_2O_4$/g-C_3N_4 nanocomposites (DZG1, DZG2, and DZG3) with 10 ppm RhB dye for 75 min irradiation time. The effects of varying H_2O_2 concentrations from 2 to 14 mM on RhB photodegradation were observed, as shown in Figure 7(c). When H_2O_2 dosage was increased from 2 to 6 mM, RhB removal efficiency increased correspondingly from 71% to 95.5% for Dy^{3+} doped $ZnFe_2O_4$/g-C_3N-X (X = 0.2, 0.3, 0.4). Increasing the concentration of H_2O_2 in RhB The formation of (•OH) radicals was enhanced by the dye solution critical for the degradation process [45].

The effect of irradiation time on degradation (%) at optimum conditions was analyzed and represented in Figure 7(d). By taking samples out of the dye solution at various times, the percentage of degradation was determined. A noticeable increase in RhB degradation was observed in the early phases of irradiation. Over time, the rate of breakdown decreases. RhB requires a specific amount of time to be fully degraded by the catalyst's active site. This is because the pH of the solution affects the generation of (•OH) radicals, which causes the degradation rate in removal processes to progressively slow down [46]. When the process is just getting started, these radicals are essential for the breakdown of RhB molecules. However, the rate of degradation slows down as the irradiation increases. The slow saturation of the catalyst's active sites and the loss of easily accessible RhB molecules in the solution are the causes of this decrease.

A photocatalyst's stability and reusability must be examined from an economic and environmental perspective. After completing the degradation reaction, the composites were recovered using a magnet, washed three times with distilled water and oven-dried at 80 °C. Once dried, the composites were reused for subsequent cycles. Every composite undergoes a reusability study at the same optimal conditions, such as pH 8, oxidant dose 8 milli M and composite dosage 40 mg/50 mL for tested samples (DZG1, DZG2, and DZG3). Figure 7(e) shows that the photocatalyst can be reused up to five times while maintaining 84% photocatalytic activity and causing little loss in product yield.

4.7. Kinetics of photodegradation reaction

The experimental data of Dy^{3+} doped $ZnFe_2O_4$/g-C_3N_4 nanocomposites (DZG1, DZG2, and DZG3) composites was analyzed using the pseudo first-order kinetic model for the quantitative investigation of RhB degradation shown in Figure 7(f). The Equation (24) is specifically created for photocatalytic studies when the pollutant concentration is taken in the millimolar range.

$$\ln\frac{C_0}{C_t} = -kt \tag{24}$$

Figure 8 shows a linear relationship between ln (C_0/C_t) and reaction time. Where C_t is the final concentration of RhB at time t and C_0 is the initial concentration degradation of RhB by ternary and binary composites following first order. The first-order R^2 values for DZG1, DZG2, and DZG3 composites are 0.9336, 0.9453, and 0.9426, respectively. The reaction rate constants and R^2 values for Rhodamine B (RhB) degradation are shown in Table 4. A detailed comparison of photocatalysis of the current work with previously reported work is given in Table 5.

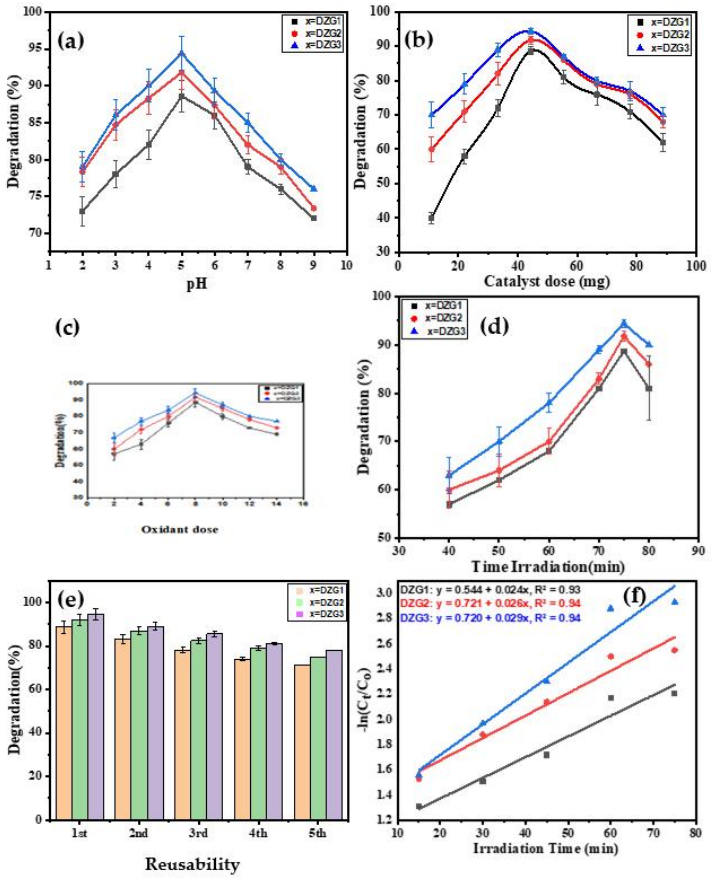

Figure 7. Effects of (a) pH; (b) catalyst dose; (c) oxidant dose; (d) irradiation time; (e) reusability; (f) first-kinetic model of Dy^{3+} doped $ZnFe_2O_4$/g-C_3N_4 nanocomposites (DZG1, DZG2, and DZG3) on degradation efficiency.

Table 4. Kinetic model fitting of first order for RhB degradation using composites.

Photocatalyst	K (min^{-1}) 1st order	R^2 value for pseudo-1st order
DZG1	0.00036	0.9336
DZG2	0.00032	0.9453
DZG3	0.00029	0.9426

Table 5. Comparison of photocatalytic performance of the current work with reported literature.

Material/Composite	Dye used	Degradation time (min)	Efficiency (%)	Reference
$ZnFe_2O_4$/ZnO	Congo red	75	93	[47]
$ZnFe_2O_4$/CdS-GO	RhB	40	82	[48]
$ZnFe_2O_4$/$CoFe_2O_4$	MB	180	100	[23]
$ZnFe_2O_4$/Ag	tetracycline	80	90	[18]
$ZnFe_2O_4$/CdS	RhB	60	93	[49]
$ZnFe_2O_4$/CNTs	RhB	120	72	[21]
$ZnFe_2O_4$/WO_3	Crystal Violet	45	90	[50]
$ZnFe_2O_4$/g-C_3N_4	Uranium	90	94.62	[51]
Dy^{3+}-$ZnFe_2O_4$/g-C_3N_4	RhB	75	96.5	Present work

4.8. Photodegradation mechanism

A photocatalytic mechanism is illustrated in Figure 8. As illustrated in Figure 8, Dy^{3+} ions introduce intermediate 4f energy levels within the $ZnFe_2O_4$/g-C_3N_4 heterojunction, acting as electron-trapping and transfer centers. These localized energy states facilitate interfacial charge migration from $ZnFe_2O_4$ to g-C_3N_4, suppress reverse electron transfer, and significantly reduce electron-hole recombination. Consequently, the prolonged charge-carrier lifetime enhances the generation of reactive oxygen species (•OH and $•O_2^-$), leading to improved RhB photodegradation efficiency. When there is visible light, the movement of electrons (e-) from $ZnFe_2O_4$ to g-C_3N_4 and the transfer of holes (h^+) from g-C_3N_4 to $ZnFe_2O_4$ occur through Dy^{3+} as an electron mediator. In this process, the valence band holes of $ZnFe_2O_4$ and conduction band electrons of g-C_3N_4 undergo charge transference through a conventional heterojunction mechanism. The photoinduced holes in the valance band (VB) of $ZnFe_2O_4$ are absorbed through, using H_2O to produce •OH radicals. Additionally, the photoinduced electrons in the conduction band (CB) of g-C_3N_4 are captured by dissolved oxygen. Consequently, the $•O_2$ anion reacts with H_2O_2 to generate the hydroxyl radical, which efficiently degrades the RhB dye. RhB breaks down into certain inorganic ions, CO_2, and H_2O. Therefore, it suggests using the Dy^{3+}-doped $ZnFe_2O_4$/g-C_3N_4 composite as a photocatalyst due to its high photocatalytic activity, longer charge-carrier lifetime, and higher charge-separation efficiency. Specifically, Dy^{3+} can promote electron transfer from $ZnFe_2O_4$ to g-C_3N_4 and suppress the reverse transfer to $ZnFe_2O_4$. Consequently, the photoactivity of Dy^{3+} doped $ZnFe_2O_4$ with g-C_3N_4 was significantly improved. Some steps involved in this process are given:

$$ZnFe_2O_4 + hv(\text{Visible}) \rightarrow h_{VB}^+ + e_{CB}^- \quad (25)$$

$$g - C_3N_4 + hv(\text{Visible}) \rightarrow h_{VB}^{+} + e_{CB}^{-} \quad (26)$$

$$e_{CB}^{-}(ZnFe_2O_4) \rightarrow Dy^{3+} \rightarrow e_{CB}^{-}(g - C_3N_4) \quad (27)$$

$$e_{CB}^{-} + O_2 \rightarrow \cdot O_2^{-} \quad (28)$$

$$\cdot O_2^{-} + H^{+} \rightarrow \cdot HO_2 \quad (29)$$

$$H_2O_2 + e_{CB}^{-} \rightarrow \cdot OH + OH^{-} \quad (30)$$

$$H_2O + h_{VB}^{+} \rightarrow \cdot OH + H^{+} \quad (31)$$

$$OH^{-} + h_{VB}^{+} \rightarrow \cdot OH \quad (32)$$

$$ROS + RhB \rightarrow CO_2 + H_2O \quad (33)$$

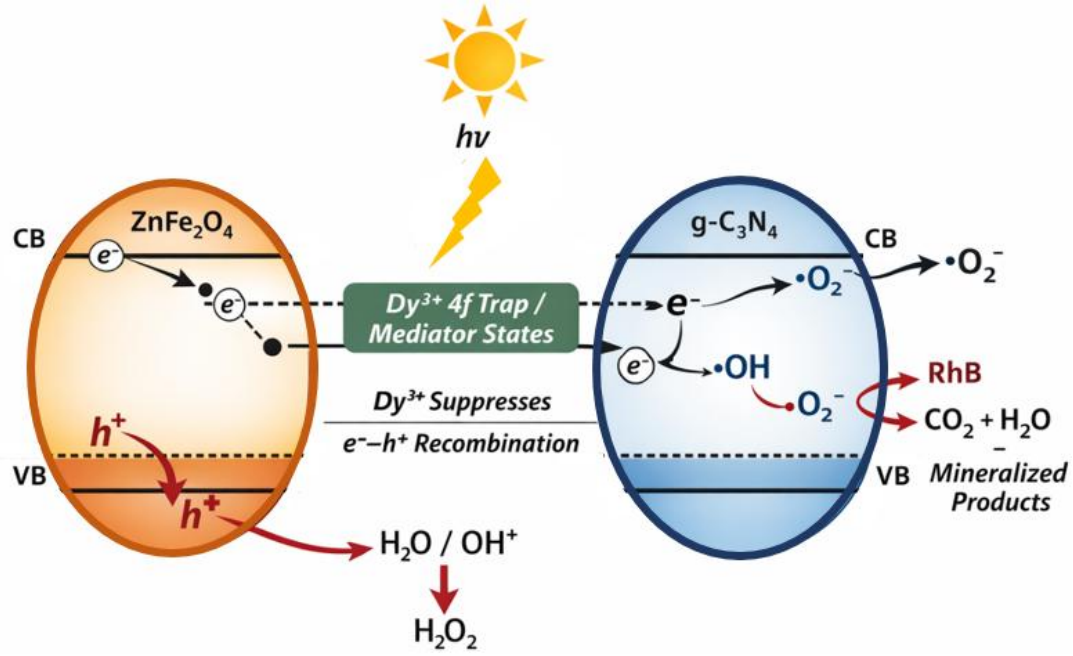

Figure 8. Schematic diagram of photocatalytic activity.

5. Conclusion

This study presents the novel application of Dy^{3+}-doped $ZnFe_2O_4$ supported on g-C_3N_4 as an efficient electron-mediated photocatalyst for dye degradation under solar light irradiation. Dy^{3+}-doped $ZnFe_2O_4$/g-C_3N_4 nanocomposites (DZG1, DZG2, and DZG3) were successfully synthesized via a simple co-precipitation method and systematically characterized using XRD, SEM/EDX, FTIR, UV-Vis spectroscopy, and dielectric analyses. Structural investigations confirmed the formation of a cubic spinel $ZnFe_2O_4$ phase, while morphological studies revealed improved particle dispersion upon g-C_3N_4 incorporation. Dielectric studies exhibited pronounced frequency-dependent behavior, with variations in dielectric constant, dielectric loss, and tangent loss, indicating enhanced charge transport and polarization effects that support efficient photocatalytic activity. Among the synthesized composites, the DZG3 sample demonstrated superior photocatalytic performance, achieving 96.5% RhB degradation within 75 min under optimized conditions, including pH 8, a catalyst dosage of 40 mg/100 mL, and an H_2O_2 concentration of 8 mM. Compared to DZG1 and DZG2, the enhanced activity of DZG3 is attributed to improved visible-light absorption, efficient charge separation, and the electron mediator role of

Dy^{3+} ions at the $ZnFe_2O_4$/g-C_3N_4 interface. Furthermore, the Dy^{3+}-doped $ZnFe_2O_4$/g-C_3N_4 composites exhibited good durability, magnetic recoverability, and reusability, highlighting their potential for practical environmental remediation applications. The facile synthesis route and stable photocatalytic performance underscore the feasibility of this material system for scalable wastewater treatment. Overall, this work demonstrates an effective strategy to enhance the photo-efficiency and recyclability of g-C_3N_4-based photocatalysts through rare-earth-mediated heterojunction engineering, with the DZG3 (x = 0.4) composite showing the most promising performance.

Acknowledgments: Not applicable.

Availability of Data and Materials: Data will be made available on request.

Funding: This research received no external funding.

Author Contributions: SA contributed to the experiments, software, formal analysis, writing-original draft, and editing; HA contributed to the supervision, conceptualization, project management, and writing-review; KA and MZ contributed by providing resources and writing-review. All authors have read and approved the final manuscript. All authors contributed to editorial changes in the manuscript. All authors have participated sufficiently in the work and agreed to be accountable for all aspects of the work.

Conflicts of Interest: The authors declare that they have no known competing financial interests or personal relationships that could have appeared to influence the work reported in this paper.

References

1. Gong, A.Q.; Ping, W.H.; Wang, J.; et al. Cyclodextrin polymer/Fe_3O_4 nanocomposites as solid phase extraction material coupled with UV–vis spectrometry for the analysis of rutin. *Spectrochimica Acta Part A: Molecular and Biomolecular Spectroscopy* 2014, 122, 331–336. https://doi.org/10.1016/j.saa.2013.11.050
2. Mäki, A.; Valkealahti, S. Differentiation of multiple maximum power points of partially shaded photovoltaic power generators. *Renewable Energy* 2014, 71, 89–99. https://doi.org/10.1016/j.renene.2014.05.018
3. Sahinkaya, E.; Gungor, M.; Bayrakdar, A.; et al. Separate recovery of copper and zinc from acid mine drainage using biogenic sulfide. *Journal of Hazardous Materials* 2009, 171(1–3), 901–906. https://doi.org/10.1016/j.jhazmat.2009.06.089
4. Oueslati, M.H.; Tahar, L.B.; Harrath, A.H. Catalytic, antioxidant and anticancer activities of gold nanoparticles synthesized by kaempferol glucoside from Lotus leguminosae. *Arabian Journal of Chemistry* 2020, 13(1), 3112–3122. https://doi.org/10.1016/j.arabjc.2018.09.003
5. Zhu, Q.J.; Cai, Z.W.; Zhou, P.L.; Sun, X.X.; Xu, J. Recent progress of membrane technology for chiral separation: A comprehensive review. *Separation and Purification Technology* 2023, 309, 123077. https://doi.org/10.1016/j.seppur.2022.123077
6. Sharma, J.; Singh, H.; Sharma, S.; et al. Rhodamine B induced alteration in antioxidant enzymes and photosynthetic performance of Eichhornia crassipes. *Plant Physiology Reports* 2022, 27, 603–617. https://doi.org/10.1007/s40502-022-00688-3
7. Irfan, M.; Zahid, M.; Tahir, N.; et al. Enhanced photo-Fenton degradation of Rhodamine B using iodine-doped iron tungstate nanocomposite under sunlight. *International Journal of Environmental Science and Technology* 2023, 20, 3645–3660. https://doi.org/10.1007/s13762-022-04216-6
8. Nastasiienko, N.; Palianytsia, B.; Kartel, M.; Larsson, M.; Kulik, T. Thermal Transformation of Caffeic Acid on the Nanoceria Surface Studied by Temperature Programmed Desorption Mass-Spectrometry, Thermogravimetric Analysis and FT – IR Spectroscopy. *Colloids Interfaces* 2019, 3, 34. https://doi.org/10.3390/colloids3010034
9. Peng, J.H.; Guo, J.H.; Lv, S.X.; et al. Novel $ZnFe_2O_4$@MnO_2@MXene composites with ultrathin thickness and excellent electromagnetic absorption performance. *Composites Communications* 2022, 35, 101316. https://doi.org/10.1016/j.coco.2022.101316
10. Fu, W.L.; Xu, Y.H.; Yan, B.; et al. Numerical simulation of local doped barrier layer AlGaN/GaN HEMTs. *Superlattices and Microstructures* 2013, 60, 443–452. https://doi.org/10.1016/j.spmi.2013.05.017

11. Alraae, A.; Moussadik, A.; Benzaouak, A.; et al. One-step eco-friendly synthesis of Ag nanoparticles on bentonite-g-C_3N_4 for the reduction of hazardous organic pollutants in industrial wastewater. *Next Nanotechnology* 2025, 7, 100116. https://doi.org/10.1016/j.nxnano.2024.100116
12. Bhattacharjee, N.; Som, I.; Saha, R.; et al. A critical review on novel eco-friendly green approach to synthesize zinc oxide nanoparticles for photocatalytic degradation of water pollutants. *International Journal of Environmental Analytical Chemistry* 2024, 104, 489–516. https://doi.org/10.1080/03067319.2021.2022130
13. Aridi, A.; Naoufal, D.; El-Rassy, H.; et al. Photocatalytic activity of $ZnFe_2O_4$/NiO nanocomposites carried out under UV irradiation. *Ceramics International* 2022, 48, 30905–30916. https://doi.org/10.1016/j.ceramint.2022.07.046
14. Alraae, A.; Moussadik, A.; Benzaouak, A.; El Hazzat, M.; Kacimi, M.; Dahhou, M.; Sifou, A.; El Hamidi, A. Cu nanoparticles-decorated beidellite: Synthesis, characterization, and catalytic reduction of wastewater pollutants. *Colloids and Surfaces A: Physicochemical and Engineering Aspects* 2025, 718, 136885. https://doi.org/10.1016/j.colsurfa.2025.136885
15. Alraae, A.; Hussain, R.; Moussadik, A.; Benzaouak, A.; Karim, S.; Kacimi, M.; Bellaouchou, A.; Bentata, F.; Dahhou, M.; Sifou, A.; El Hamidi, A.; et al. Eco-friendly fabrication and multifunctional evaluation of silver-doped muscovite-g-C3N4 nanocomposites for catalytic and antimicrobial applications. *Colloids and Surfaces A: Physicochemical and Engineering Aspects* 2026, 728, 138675. https://doi.org/10.1016/j.colsurfa.2025.138675
16. Shen, Z.G.; Peng, Z.J.; Zhao, Z.Y.; et al. Nonlinear current-voltage characteristics of WO_{3-x} nano-/micro-rods. *Solid State Sciences* 2018, 78, 126–132. https://doi.org/10.1016/j.solidstatesciences.2018.03.002
17. Alraae, A.; Moussadik, A.; Benzaouak, A.; et al. Eco-friendly synthesis and catalytic activity of Cu nanoparticles deposited on expanded muscovite to reduce organic pollutants. *Results in Surfaces and Interfaces* 2024, 17, 100343. https://doi.org/10.1016/j.rsurfi.2024.100343
18. Huerta-Aguilar, C.A.; Diaz-Puerto, Z.J.; Tecuapa-Flores, E.D.; et al. Crystal plane impact of $ZnFe_2O_4$–Ag nanoparticles influencing photocatalytical and antibacterial properties: Experimental and theoretical studies. *ACS Omega* 2022, 7, 33985–34001. https://doi.org/10.1021/acsomega.2c03153
19. Sabzehmeidani, M.M.; Karimi, H.; Ghaedi, M.; et al. Construction of efficient and stable ternary $ZnFe_2O_4$/Ag/AgBr Z-scheme photocatalyst based on $ZnFe_2O_4$ nanofibers under LED visible light. *Materials Research Bulletin* 2021, 143, 111449. https://doi.org/10.1016/j.materresbull.2021.111449
20. Hou, Y.; Li, X.Y.; Zhao, Q.D.; et al. Electrochemical method for synthesis of a $ZnFe_2O_4$/TiO_2 composite nanotube array modified electrode with enhanced photoelectrochemical activity. *Advanced Functional Materials* 2010, 20, 2165–2174. https://doi.org/10.1002/adfm.200902390
21. Wang, Y.H.; Lu, Z.H.; Wu, S.; et al. Boosting electrocatalytic performance of $ZnFe_2O_4$/CNT via synergy of CNT defect and oxygen vacancies. *Journal of Environmental Chemical Engineering* 2024, 12, 112839. https://doi.org/10.1016/j.jece.2024.112839
22. Nejad, Z.K.; Mirzaei-Kalar, Z.; Khandar, A.A. Synthesis of $ZnFe_2O_4$@SiO_2 nanoparticles as a pH-sensitive drug release system and good nanocarrier for CT-DNA binding. *Journal of Molecular Liquids* 2021, 339, 117155. https://doi.org/10.1016/j.molliq.2021.117155
23. Anju, A.; Yadav, R.S.; Kuřitka, I.; et al. Lightweight, flexible and high-performance nanocomposites based on reduced graphene oxide and spinel ferrite ($ZnFe_2O_4$/$CoFe_2O_4$) nanoparticles in thermoplastic polyurethane matrix for electromagnetic interference shielding applications. In: Proceedings of the 13th International Conference on Nanomaterials—Research and Application; October 20–22, 2021; Brno, Czech Republic. pp 59–64.
24. Holzwarth, U.; Gibson, N. The Scherrer equation versus the 'Debye–Scherrer equation'. *Nature Nanotechnology* 2011, 6(9), 534. https://doi.org/10.1038/nnano.2011.145
25. Naseri, M.; Kamalianfar, A.; Naderi, E.; et al. The effect of Ag nanoparticles on physical and photocatalytic properties of $ZnFe_2O_4$/SiO_2 nanocomposite. *Journal of Molecular Structure* 2020, 1206, 127706. https://doi.org/10.1016/j.molstruc.2020.127706
26. Glasser, L.; Jenkins, H.D.B. Lattice energies and unit cell volumes of complex ionic solids. *Journal of the American Chemical Society* 2000, 122, 632–638. https://doi.org/10.1021/ja992375u

27. Bose, A.K.; Zhang, X.; Maddipatla, D.; et al. Highly sensitive screen printed strain gauge for micro-strain detection. In: Proceedings of the 2019 IEEE International Conference on Flexible and Printable Sensors and Systems (FLEPS); 7–10 July, 2019; Glasgow, United Kingdom. pp 1–3.
28. Li, M.C.; Li, R.S.; Zhang, T.S. Phase equilibria of SiO_2–Ce_2O_3–CaO-25 wt% Al_2O_3 system at 1673 K–1773 K. *Ceramics International* 2022, 48(21), 31614–31626. https://doi.org/10.1016/j.ceramint.2022.07.083
29. Vinosha, P.A.; Vinsla, J.V.A.; Madhavan, J.; et al. Impact of dysprosium doped (Dy) zinc ferrite ($ZnFe_2O_4$) nanocrystals in photo-fenton exclusion of recalcitrant organic pollutant. *Environmental Research* 2022, 203, 111913. https://doi.org/10.1016/j.envres.2021.111913
30. Ge, L.; Han, C.C.; Liu, J.; et al. Enhanced visible light photocatalytic activity of novel polymeric g-C_3N_4 loaded with Ag nanoparticles. *Applied Catalysis A: General* 2011, 409–410, 215–222. https://doi.org/10.1016/j.apcata.2011.10.006
31. Mandru, A.; Mane, J.; Mandapati, R. A review on UV-visible spectroscopy. *Journal of Pharma Insights and Research* 2023, 1(2), 91–96. http://jopir.in/index.php/journals/article/view/42
32. Rocha, F.S.; Gomes, A.J.; Lunardi, C.N.; et al. Experimental methods in chemical engineering: Ultraviolet visible spectroscopy—UV-Vis. *Canadian Journal of Chemical Engineering* 2018, 96(12), 2512–2517. https://doi.org/10.1002/cjce.23344
33. Souri, D.; Tahan, Z.E. A new method for the determination of optical band gap and the nature of optical transitions in semiconductors. *Applied Physics B* 2015, 119, 273–279. https://doi.org/10.1007/s00340-015-6053-9
34. Shabbir, A.; Sardar, S.; Mumtaz, A. Mechanistic investigations of emerging type-II, Z-scheme and S-scheme heterojunctions for photocatalytic applications–A review. *Journal of Alloys and Compounds* 2024, 1003, 175683. https://doi.org/10.1016/j.jallcom.2024.175683
35. Sundararajan, M.; Sukumar, M.; Dash, C.S.; et al. A comparative study on $NiFe_2O_4$ and $ZnFe_2O_4$ spinel nanoparticles: Structural, surface chemistry, optical, morphology and magnetic studies. *Physica B: Condensed Matter* 2022, 644, 414232. https://doi.org/10.1016/j.physb.2022.414232
36. Müller, H.; Strubel, C.; Bange, K. Characterization and identification of local defects in glass. *Scanning* 2001, 23(1), 14–23. https://doi.org/10.1002/sca.4950230103
37. Ola, O.; Maroto-Valer, M.M. Review of material design and reactor engineering on TiO_2 photocatalysis for CO_2 reduction. *Journal of Photochemistry and Photobiology C: Photochemistry Reviews* 2015, 24, 16–42. https://doi.org/10.1016/j.jphotochemrev.2015.06.001
38. Koe, W.S.; Lee, J.W.; Chong, W.C.; et al. An overview of photocatalytic degradation: photocatalysts, mechanisms, and development of photocatalytic membrane. *Environmental Science and Pollution Research* 2020, 27, 2522–2535. https://doi.org/10.1007/s11356-019-07193-5
39. Latif, M.; Aziz, M.H.; Shaheen, F.; et al. Enhanced photocatalysis activity of $Co_{0.5}Mg_{0.5}Fe_2O_4$/rGO nanocomposites for tetracycline antibiotic degradation. *Materials Letters* 2024, 360, 135756. https://doi.org/10.1016/j.matlet.2023.135756
40. Dang, Z.; Fan, L.; Zhao, S.; et al. Dielectric properties and morphologies of composites filled with whisker and nanosized zinc oxide. *Materials Research Bulletin* 2003, 38 (3), 499 – 507. https://doi.org/10.1016/S0025-5408(02)01055-3
41. Haseena, A.P.; Unnikrishnan, G.; Kalaprasad, G. Dielectric properties of short sisal/coir hybrid fibre reinforced natural rubber composites. *Composite Interfaces* 2007, 14(7-9), 763 – 775. https://doi.org/10.1163/156855407782106582
42. Drown, E.K.; Mohanty, A.K.; Parulekar, Y.; et al. The surface characteristics of organoclays and their effect on the properties of poly (trimethylene terephthalate) nanocomposites. *Composites Science and Technology* 2007, 67(15–16), 3168–3175. https://doi.org/10.1016/j.compscitech.2007.04.011
43. Bolivar, P.H.; Brucherseifer, M.; Rivas, J.G.; et al. Measurement of the dielectric constant and loss tangent of high dielectric-constant materials at terahertz frequencies. *IEEE Transactions on Microwave Theory and Techniques* 2003, 51, 1062–1066. https://doi.org/10.1109/TMTT.2003.809693
44. Zahid, Z.; Rauf, A.; Javed, M.; et al. Photocatalytic reduction of Cr(VI) to Cr(III) and photocatalytic degradation of methylene blue and antifungal activity of Ag/TiO_2 composites synthesized via the template induced route. *Inorganics* 2023, 11, 133. https://doi.org/10.3390/inorganics11030133
45. Zahid, M.; Khan, Z.U.H.; Sabahat, S.; et al. Photocatalytic degradation of Norfloxacin using biochar supported nZVMn/TiO_2 nanocomposite: Synthesis, characterization, and performance evaluation. *Surfaces and Interfaces* 2025, 72, 107034. https://doi.org/10.1016/j.surfin.2025.107034

46. Zahid, M.; Ullah, T.; Ayaz, A. Innovative nanomaterials for solar-driven photocatalysis: Harnessing light for energy and environmental remediation. *Pakistan Journal of Medical and Cardiological Review* 2026, 5(1), 51–66. https://doi.org/10.64105/mjpswd28
47. Zouhier, M.; Tanji, K.; Navío, J.A.; et al. Preparation of $ZnFe_2O_4$/ZnO composite: effect of operational parameters for photocatalytic degradation of dyes under UV and visible illumination. *Journal of Photochemistry and Photobiology A: Chemistry* 2020, 390, 112305. https://doi.org/10.1016/j.jphotochem.2019.112305
48. Miao, Z.C.; Tian, Y.H.; Li, S.Y.; et al. Photocatalytic degradation of Rhodamine B over popcorn-like $ZnFe_2O_4$/CdS–GO ternary composite. *Journal of Materials Research and Technology* 2022, 21, 1863–1877. https://doi.org/10.1016/j.jmrt.2022.10.035
49. Fang, S.S.; Zhou, Y.W.; Zhou, M.; et al. Facile synthesis of novel $ZnFe_2O_4$/CdS nanorods composites and its efficient photocatalytic reduction of Cr(VI) under visible-light irradiation. *Journal of Industrial and Engineering Chemistry* 2018, 58, 64–73. https://doi.org/10.1016/j.jiec.2017.09.008
50. Das, K.K.; Sahoo, D.P.; Mansingh, S.; et al. $ZnFe_2O_4$@WO_{3-X}/polypyrrole: An efficient ternary photocatalytic system for energy and environmental application. *ACS Omega* 2021, 6, 30401–30418. https://doi.org/10.1021/acsomega.1c03705
51. Dai, Z.R.; Zhen, Y.; Sun, Y.S.; et al. $ZnFe_2O_4$/g-C_3N_4 S-scheme photocatalyst with enhanced adsorption and photocatalytic activity for uranium(VI) removal. *Chemical Engineering Journal* 2021, 415, 129002. https://doi.org/10.1016/j.cej.2021.129002